Title

REFAME: Rain Estimation Using Forward-Adjusted Advection of Microwave Estimates

Authors

Behrangi, Ali
Imam, Bisher
Hsu, Kuolin
et al.

State of the Science of Precipitation

SPECIAL COLLECTION

REFAME: Rain Estimation Using Forward-Adjusted Advection of Microwave Estimates

ALI BEHRANGI,* BISHER IMAM, KUOLIN HSU, AND SOROOSH SOROOSHIAN

Center for Hydrometeorology and Remote Sensing, The Henry Samueli School of Engineering, and Department of Civil and Environmental Engineering, University of California, Irvine, Irvine, California

TIMOTHY J. BELLERBY

University of Hull, Hull, United Kingdom

GEORGE J. HUFFMAN

NASA GSFC Laboratory for Atmospheres and Science Systems and Applications, Inc., Greenbelt, Maryland

ABSTRACT

A new multiplatform multisensor satellite rainfall estimation technique is proposed in which sequences of Geostationary Earth Orbit infrared (GEO-IR) images are used to advect microwave (MW)-derived precipitation estimates along cloud motion streamlines and to further adjust the rainfall rates using local cloud classification. The main objective of the Rain Estimation using Forward-Adjusted advection of Microwave Estimates (REFAME) is to investigate whether inclusion of GEO-IR information can help to improve the advected MW precipitation rate as it gets farther in time from the previous MW overpass. The technique comprises three steps. The first step incorporates a 2D cloud tracking algorithm to capture cloud motion streamlines through successive IR images. The second step classifies cloudy pixels to a number of predefined clusters using brightness temperature (Tb) gradients between successive IR images along the cloud motion streamlines in combination with IR cloud-top brightness temperatures and textural features. A mean precipitation rate for each cluster is calculated using available MW-derived precipitation estimates. In the third step, the mean cluster precipitation rates are used to adjust MW precipitation intensities advected between available MW overpasses along cloud motion streamlines. REFAME is a flexible technique, potentially capable of incorporating diverse precipitation-relevant information, such as multispectral data. Evaluated over a range of spatial and temporal scales over the conterminous United States, the performance of the full REFAME algorithm compared favorably with products incorporating either no cloud tracking or no intensity adjustment. The observed improvements in root-mean-square error and especially in correlation coefficient between REFAME outputs and ground radar observations demonstrate that the new approach is effective in reducing the uncertainties and capturing the variation of precipitation intensity along cloud advection streamlines between MW sensor overpasses. An extended REFAME algorithm combines the adjusted advected MW rainfall rates with infrared-derived precipitation rates in an attempt to capture precipitation events initiating and decaying during the interval between two consecutive MW overpasses. Evaluation statistics indicate that the extended algorithm is effective to capture the life cycle of the convective precipitation, particularly for the interval between microwave overpasses in which precipitation starts or ends.

* Current affiliation: Jet Propulsion Laboratory, California Institute of Technology, Pasadena, California.

Corresponding author address: Ali Behrangi, Jet Propulsion Laboratory, California Institute of Technology, 4800 Oak Grove Dr., MS 183-301, Pasadena, CA 91109.
E-mail: ali.behrangi@jpl.nasa.gov

1. Introduction

High-quality precipitation data at fine time and space resolution have many hydrometeorological applications including flood forecasting, drought monitoring, disaster management, and initialization of numerical weather prediction models, among others. The current constellation of earth observing satellites allows global retrieval

of precipitation data that complement ground precipitation observations from relatively sparse radar/gauge networks. While high-resolution precipitation remote sensing is gaining popularity within several scientific communities, it faces many challenges. The main challenge is not only to derive high-quality precipitation intensity from each individual sensor, but also to combine information from different sensors in order to improve consistency, accuracy, coverage, and timeliness of high-resolution precipitation estimation. Currently, the two most commonly used types of sensors in space-based precipitation monitoring are passive microwave (MW) and infrared (IR) sensors. Microwave sensors, which are so far available only aboard Low Earth Orbit (LEO) satellites, are sensitive to cloud hydrometeors and yield relatively accurate instantaneous precipitation estimates for those times when the satellite passes over a given geographical region. On the other hand, IR sensors aboard Geostationary Earth Orbit (GEO) satellites can only image clouds rather than the hydrometeors they contain. GEO satellite data alone yield relatively inaccurate rainfall intensity estimates that nonetheless provide comprehensive spatial and temporal coverage. Given that in the latter case, precipitation is indirectly estimated from cloud forms present in frequent GEO images, attempts to combine GEO-IR estimates with the less frequent but higher-quality precipitation information from LEO-MW data has been a major research issue for more than a decade. These efforts, which will significantly benefit from the anticipated launch and operation of the National Aeronautics and Space Administration (NASA) Global Precipitation Measurement (GPM) mission, can be categorized into four major groups.

The first and most common type of IR–MW combination approach includes techniques that retrieve precipitation intensity by establishing an empirical relationship between GEO-IR images and microwave precipitation estimates to yield an improved, locally calibrated function mapping IR imagery to surface rainfall rates. This includes (i) methods that use microwave estimates to adjust an IR threshold for rain area delineation followed by rain-rate estimation (Adler et al. 1993; Kummerow and Giglio 1995; Xu et al. 1999), (ii) probability/histogram matching methods in which the cumulative distribution functions of MW rain rates and IR brightness temperatures are matched to provide IR-rain-rate equations under the general assumption that colder clouds statistically produce more intense rainfall (Hong et al. 2004; Huffman et al. 2007; Kidd et al. 2003; Sorooshian et al. 2000; Todd et al. 2001; Turk et al. 2000), and (iii) regression methods in which MW estimates are directly related to coincident IR pixel data to establish a regression-based equation for rain-rate estimation (Kuligowski 2002;

Martin et al. 1990; Miller et al. 2001; Vicente et al. 1998). As discussed by Kidd et al. (2003), calibration-based combination strategies are affected by the inherent trade-off between the temporal and spatial details of the calibration domain. A longer calibration time scale allows for better retention of spatial details but at the expense of short-term variation in the IR–rainfall relationship. Conversely, when calibration uses coincident MW–IR images, the algorithm can better capture short-term variability of IR–rainfall relationships, but at the expense of information regarding their spatial variability because of the limited number or coincident samples.

A second combination strategy, which may be used in concert with the first, focuses on obtaining the "best" local estimate for a given grid box. This approach has been employed for generating robust medium-resolution precipitation products as opposed to finer temporal resolution time series. The 3B42-RT product of the Tropical Rainfall Measuring Mission (TRMM) Multisatellite Precipitation Analysis (TMPA; Huffman et al. 2007) relies on collecting available MW estimates from various satellites within a time bracket of 3 h for each cell on a $0.25° \times 0.25°$ grid and then filling gaps in the grid with MW-calibrated IR estimates. Clearly, the fundamental differences between what IR and MW instruments observe may affect the spatial consistency of rainfall estimates, introducing discontinuities that may be problematic for studies focusing on rainfall structures. These problems can arise in other MW–IR algorithms where the discontinuities in sensor coverage translate into discontinuities in product characteristics.

Cloud motion tracking, which is increasingly becoming a common operational application of GEO satellite imagery, forms the core element of the third combination strategy. The Climate Prediction Center Morphing Method (CMORPH; Joyce et al. 2004) estimates a temporally and spatially complete precipitation field, exclusively from MW observations through guided propagation of precipitation estimates between two MW images using IR-based cloud tracking. In brief, CMORPH consists of the following steps: 1) the spatial lag correlations obtained from successively collocated IR images are used to calculate cloud motion vectors, 2) the relatively high-quality MW-derived precipitation estimates are propagated forward in time along the cloud motion vectors until the next MW overpass is reached, 3) the latter MW precipitation field is propagated backward in time using the existing motion vectors, and 4) a time-weighted linear interpolation of the MW precipitation is obtained by averaging the forward- and backward-propagated precipitation fields. The interpolation allows for modification of shape and intensity (morphing) of the precipitation field between two microwave overpasses.

CMORPH has shown good results based on evaluation statistics reported during the Pilot Evaluation of High-Resolution Precipitation Products (PEHRPP) initiative as well as in few other studies (Dinku et al. 2008; Sapiano and Arkin 2009; Tian et al. 2007). However, a few concerns can be raised. First, the morphed precipitation product relies on the MW precipitation estimates at the two ends of a cloud advection path. As such, the method is unable to capture precipitation events that may form and dissipate between two MW overpasses such as convective precipitation. More generally, CMORPH may not result in accurate estimates if the precipitation field during the morphing process varies nonlinearly.

The Global Satellite Mapping of Precipitation (GSMaP)_moving vector with Kalman filter (MVK) algorithm (Ushio et al. 2009) incorporates the frequently available GEO information in adjusting the propagated precipitation field. Although GSMaP_MVK is similar to CMORPH in propagating the MW-derived precipitation field using the IR-derived motion vectors, it differs from CMORPH in that it also uses cloud-top brightness temperatures to adjust the propagated precipitation intensities along the motion vectors. More specifically, by considering the relationship between Tb and precipitation rate and its associated uncertainties, a Kalman filter is applied to the propagated precipitation to update the IR–Tb relationship. The same Kalman gain value may be used to adjust precipitation intensities along a given motion vector in both forward- and backward-propagation stages. The final rain-rate estimate at each interval is eventually obtained after weighted averaging of the forward- and backward-propagated precipitation estimates based on the root-mean-square uncertainties associated with each stage. Note that the CMORPH group is also pursuing a Kalman filter methodology by using IR-based estimates to improve their algorithm (Joyce et al. 2008).

The combination of backward and forward propagation of MW precipitation estimates is an attempt to capture the dynamics of growing or decaying precipitation systems. However, the need for a pair of consecutive MW observations along the motion vectors, which are generally separated by a time lag up to 3 h or more, reduces the effectiveness of this approach in real-time monitoring of precipitation. Even with GPM in full operation, the revisit time between two MW overpasses will not improve significantly. Real-time precipitation monitoring at high time and space resolution is critical for extreme hydrologic events such as flash floods.

To improve real-time high-resolution estimation of precipitation rate using GEO-IR-based cloud tracking and MW data, Bellerby et al. (2009) and Hsu et al. (2009)

developed the Lagrangian Model (LMODEL) algorithm that combines a high-resolution 2D cloud tracking system (Bellerby 2006) and a conceptual semi-Lagrangian cloud model. The model estimates convective and stratiform precipitable water fluxes from GEO imagery and uses these to model bulk cloud liquid water content and associated rainfall rates as they evolve along streamlines. Model parameters are locally adjusted at MW overpasses and these adjustments are interpolated along streamlines between overpasses. State variables are sequentially updated using a Kalman filter at each MW overpass. The method has been tested under the conterminous United States and has been demonstrated to be effective at capturing rainfall variability between MW overpasses. A weakness of the current LMODEL algorithm is that is does not contain any mechanism to distinguish between cloud types.

In this study, we propose a new tracking-based MW–IR rainfall estimation approach that incorporates cloud classification to improve real-time precipitation estimation. The Rain Estimation using Forward-Adjusted advection of Microwave Estimates (REFAME) algorithm computes cloud motion vectors from frequent GEO-IR cloud-top images using the method developed by Bellerby (2006). Calculated temperature gradients between successive Tb images along with other textural and brightness temperature features are then used to classify GEO satellite grid boxes into a predetermined number of clusters. Mean precipitation rates for each cluster are then derived from time–space-matched MW-derived precipitation rates in manners similar to the recently reported Precipitation Estimation from Remotely Sensed Information using Artificial Neural Networks–Multispectral Analysis (PERSIANN-MSA) method (Behrangi et al. 2009b). The cluster mean precipitation rates are used to adjust the MW precipitation intensities as they are advected along cloud motion streamlines.

The datasets used in this study are described in section 2. The development and structure of the REFAME algorithm along with few other variations of the algorithm are described in section 3. The variations facilitate the evaluation of the REFAME. A detailed evaluation and comparison of the REFAME and the reference products is provided in section 4. Finally, conclusions are presented in section 5.

2. Dataset

GEO-IR data from the Climate Prediction Center (CPC) merged IR dataset (Janowiak et al. 2001) and MW-derived precipitation estimation from the CPC merged microwave dataset (Joyce et al. 2004) were obtained for a study region covering the continental United

States (CONUS) for the period June–August 2006. The CPC IR dataset is a composite of all available GEO-IR (~11 μm) images, with zenith angle corrections, and is available at 4-km spatial resolution every 30 min. The IR data were remapped onto 0.08° spatial resolution for this study. The CPC merged MW precipitation data includes data from the Defense Meteorological Satellite Program (DMSP) Special Sensor Microwave Imager (SSM/I), Polar Operational Environmental Satellite (POES) Advanced Microwave Sounding Unit-B (AMSU-B), the *Aqua* Advanced Microwave Scanning Radiometer-E (AMSR-E), and the TRMM Microwave Imager (TMI) instruments (Ferraro 1997; Ferraro et al. 2000; Kummerow et al. 2001; Weng et al. 2003). As described by Joyce et al. (2004), the merged MW precipitation data is obtained via mapping the MW precipitation estimates to the nearest grid point on rectilinear grids at ~0.07° latitude–longitude, separately for each half-hour and for each satellite. For the grids with no precipitation data, an inverse distance squared weighting interpolation of the nearest grids with precipitation estimate is used. Finally, by implementing an order of precedence in regions of overlapping sensors, a spatially complete field of merged MW precipitation estimate is obtained at ~0.07° latitude–longitude for each half-hour. Subsequently, in the present work, the merged product is interpolated to a common 0.08° spatial and 30-min temporal resolution.

The reference precipitation dataset was obtained from hourly ground-based weather radar systems, provided by the National Centers for Environmental Prediction (NCEP) and Environmental Modeling Center (EMC; Lin and Mitchell 2005). The NCEP/EMC 4-km gridded radar rainfall estimates were remapped to a 0.08° latitude–longitude grid maps, compatible with the IR and MW dataset.

In this study, the first half period (1 June–15 July 2006) dataset was used for training and calibration purpose and the rest was used to evaluate the results. The ground radar precipitation data is the reference for deriving all statistical measures for REFAME and its variations are discussed in section 4 in more detail.

3. Methodology

The REFAME technique comprises three steps. In the first step, cloud motion streamlines are captured from successive high-resolution (0.04° latitude–longitude every 30 min) IR images using a 2D cloud tracking algorithm described in section 3a. In the second step, described in section 3b, the IR grids are classified into predefined number of classes using brightness temperature (Tb) gradients between successive IR images along the cloud motion streamlines in combination with IR cloud-top brightness temperatures and textural features. Subsequently, the mean precipitation rate for each cluster is calculated using corresponding MW-derived precipitation estimates. This step is conducted using training samples prior to the testing/validation phase. In other words, during the testing/validation period the calculated mean precipitation rate for each class remains unchanged. In the third step, described in section 3c, the mean cluster precipitation rates are used to adjust MW precipitation intensities advected between available MW overpasses along cloud motion streamlines. In section 3d, a potential extension of REFAME is described in which GEO-IR-derived precipitation is averaged with REFAME-derived precipitation to account for those convective precipitations that may not be captured at the previous MW overpass.

a. High-resolution 2D cloud tracking

This study employs the high-resolution 2D cloud tracking algorithm developed by Bellerby (2006). The algorithm matches equivalent cloud pixels location between a pair of GEO-IR images using a combination of hierarchical template matching and mesh-based tracking techniques. The procedure, fully described in Bellerby (2006), consists of mapping regular mesh grid centers (nodes) of a given image (image A) to corresponding locations in the previous image (image B). The mapping starts at coarse resolution and uses localized template matching to optimize the local correspondence between the two images at and near the nodes. The mapped nodes are then connected to create a convex quadrilateral mesh over image B. Both the regular grid over image A and the irregular grid over image B are interpolated to twice their current resolution before the procedure is iterated. In this, and subsequent, iterations, the local image distortion, including rotation and shear, represented by the irregular mesh are incorporated into the local image matching process. The matching points on image B are again joined to form an irregular mesh over image B and both regular and irregular meshes interpolated to double their resolution. These steps demonstrated in Fig. 1 are then repeated until the original resolution of the Geostationary Operational Environmental Satellite (GOES) image is reached. To reduce potentially ambiguous matches, the procedure includes consistency checking, mesh untangling, and edge effect management steps. As a result, and at the end of the procedure, a Lagrangian representation of cloud development is obtained that provides, at each cloudy pixel location in image A, a translational vector that maps the pixel to its best match in image B, while explicitly incorporating the effect of cloud motion, growth, deformation,
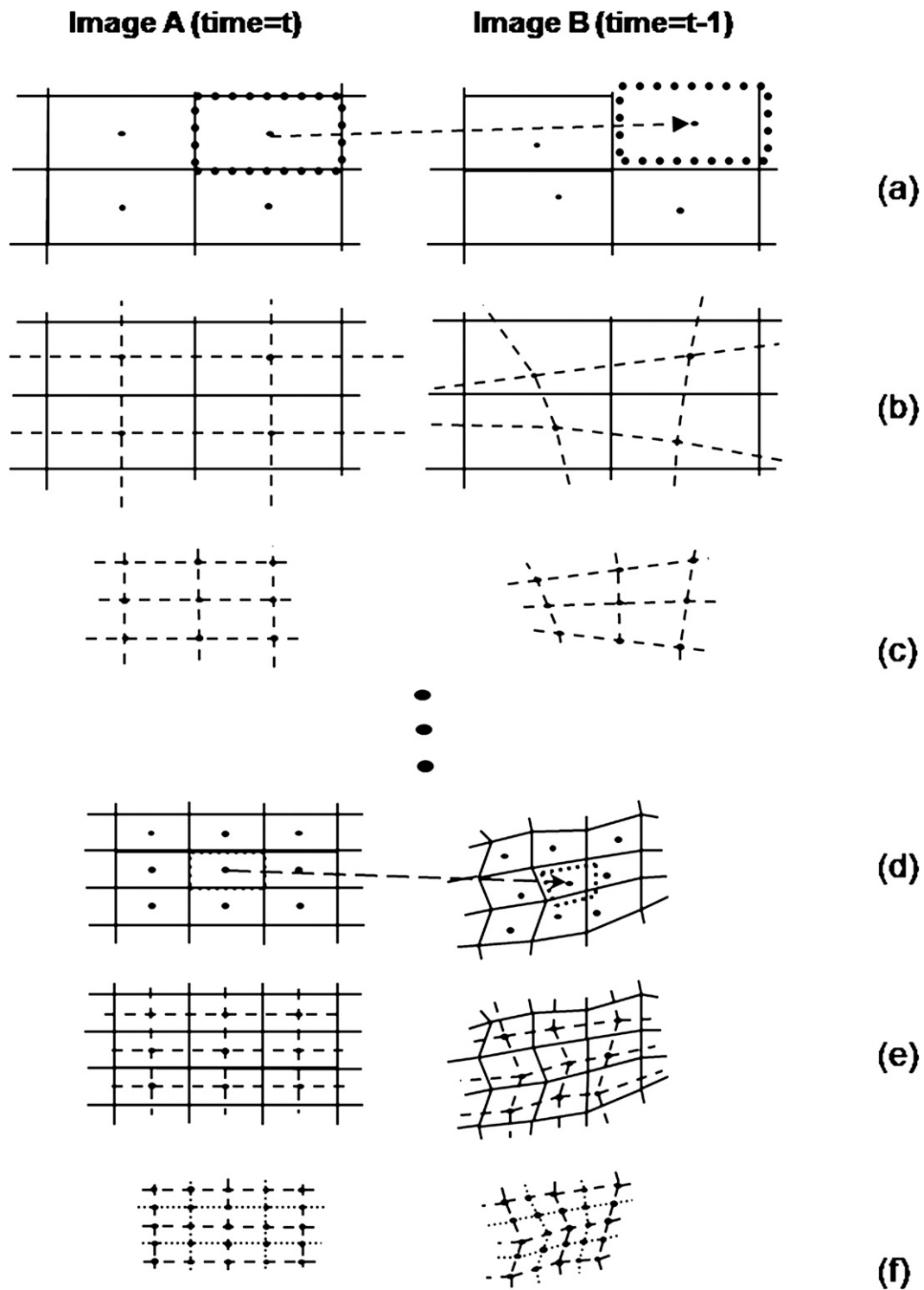
FIG. 1. Stages of the 2D cloud-advection matching algorithm (Source: Bellerby et al. 2009). (a) Correlation matching using a rectangular sliding window, (b) mesh replacement using matching results, (c) mesh interpolation, (d) correlation matching accounting for local image distortion, (e) mesh replacement using matching results, and (f) mesh interpolation.

Tb(X(t)): IR-temperature of calculation pixel at location X at time t

M3(X(t)): Mean IR-temperature of the 3x3 pixels around the calculation pixel at location X at time t

S3(X(t)): Standard deviation IR-temperature of the 3x3 pixels around the calculation pixel at location X at time t

ΔTb: Difference between M3 at time t and M3 from previous IR image at time t-1 (M3(X(t)-M3(X(t-1))
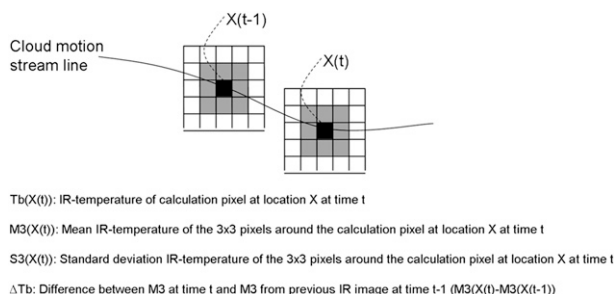
FIG. 2. Description of the GEO-IR-derived features used for classification of IR grid boxes.

and dispersal (decay). Case studies show that the algorithm is more effective and accurate in tracking cloud deformation between successive GOES images than straightforward single-stage template matching approaches (Bellerby 2006; Bellerby et al. 2009).

b. GEO input-feature extraction and classification

Because of the strong relation between Tb and cloud height, frequent high-resolution IR observations of cloud-top properties from GEO satellite images can provide information on cloud morphology, texture, and evolution, which in turn may be used to infer information relevant to precipitation intensity. For example, successive IR images may be used to detect a growing convective system where a gradient of temperature change (ΔTb) along the cloud motion streamlines is negative. A mature convective system that reaches a high elevation usually demonstrates very low cloud-top brightness temperature and small ΔTb. Stratus clouds, on the other hand, do not usually demonstrate significant ΔTb along the cloud motion streamline. They also typically appear horizontally flat in IR imagery, manifesting only insignificant changes in Tb between neighboring grid boxes.

The REFAME algorithm incorporates a range of IR-derived cloud "features" to characterize cloud types. Figure 2 illustrates the features used in REFAME including brightness temperature (Tb) of the IR grid box; texture obtained from 3×3 neighboring grid boxes: mean (M3) and standard deviation (S3); and dynamic properties, namely, Tb gradient (ΔTb) calculated from corresponding brightness temperatures at two successive images with temporal resolution of GEO-IR imagery (30 min).

The inverse statistical relationships between Tb, ΔTb (from GEO-IR), and the mean precipitation rate (from ground radar) are demonstrated in Figs. 3a,b for the three months of the study period (June, July, and August 2006). To obtain Fig. 3, Tb and ΔTb were first binned separately with a step size of two units. The mean

precipitation rate for each bin was then calculated by dividing the total volume of rain rates over the total number of samples associated with the bin. The sample count in each bin is also shown in Figs. 3c,d. The relationship between ΔTb and the mean precipitation rate suggests that in addition to Tb of each grid box, ΔTb along the cloud motion path provide useful information relevant to precipitation intensity.

The next step of the REFAME algorithm involves the classification of satellite grid boxes into a predetermined number of clusters (here, 400) sharing similar input-feature properties. The well-known k-means classification method was used herein. Briefly, the method consists of the following steps:

1) Randomly locate n cluster centers (initial centroids) within the input-feature space D.
2) Using Euclidean distance from the randomly chosen centers, assign each input-feature vector (i.e., Tb, ΔTb, M3, and S3) to the nearest center.
3) Recompute the cluster centers as the mean value of the input-feature vectors belonging to each cluster.
4) Repeat steps 2) and 3) until the cluster centers do not change within a predetermined tolerance.

The k-means clustering approach produces clusters that are located in the input-feature space D to minimize the cost, which is the sum of the squared Euclidean distance from every point in D to its nearest cluster center. The classic cost (or error) function is described as

$$E = \sum_{k=1}^{n} \sum_{x \in p_k} \|x - c_k\|^2, \qquad (1)$$

where x is a point representing an input-feature vector, C_k is the center of cluster P_k, and n is the number of clusters. Detailed information about the k-means technique is available in Duda and Hart (1973), Everitt (1993), MacQueen (1967), and Qiu and Tamhane (2007).

The classification was performed by introducing 200 000 input-feature vectors to the k-means classifier. A filtering process prior to the input-feature selection was used to sample the input-feature vectors from more than 5 million feature vectors extracted randomly from satellite pixels of the calibration period (1 June–15 July 2006). Following Behrangi et al. (2009a), the filtering process was designed to ensure that a sufficient number of clusters was maintained in the region of low Tb representing cloudy areas with a higher possibility of precipitation occurrence, resulting in a more desirable distribution of clusters in the input-feature space. The filtering process consists of three steps. First, all data samples are binned into a number of groups based on Tb (here 10 groups with unequal range). Second, the number of samples in the
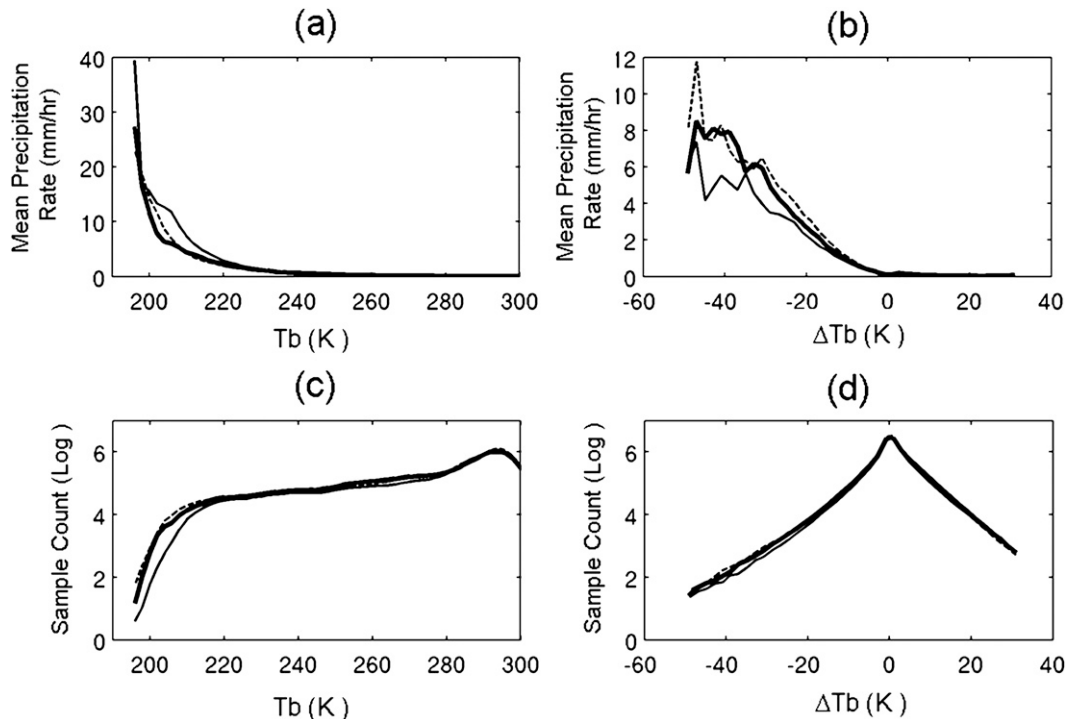
FIG. 3. Relation between Tb, ΔTb (from GEO-IR), and mean precipitation rate (from ground radar) for June (solid line), July (dark solid line), and August (dashed line) 2006 over CONUS. (a) Relation between Tb and mean precipitation rate, (b) relation Between ΔTb and mean precipitation rate, (c) number of precipitation samples in each Tb bin (with the size of 2 units) to derive the displayed relationships in (a), and (d) number of precipitation samples in each ΔTb bin (with the size of 2) to derive the displayed relationships in (b).

coldest bin is applied as an upper limit to screen the data in the other bins. Third, data from the warmer bins are randomly taken out until the total count of data vectors in each bin matches the number of samples in the coldest temperature group.

The k-means procedure is an unsupervised classification that may be performed independently of any precipitation rate observation. Classification in unsupervised mode avoids some of the difficulties that may be introduced by uncertainties in precipitation measurement field or imperfect time–space matches between satellite GEO-IR and the precipitation rate. Since the clusters are derived from multiple cloud features, the REFAME algorithm is highly flexible and capable of incorporating new inputs. Enhanced features vectors may, for example, include multispectral and cloud-patch information (Behrangi et al. 2009b; Behrangi et al. 2010).

The next stage of the REFAME algorithm involves calculating a mean precipitation rate (MPR) for each cluster using the full calibration dataset. In this stage k-means cluster centers are not changed. Input-feature vectors from each satellite grid box are calculated and used to allocate the grid box to the most closely matching cluster. If available, the corresponding MW precipitation

rate is then assigned to the cluster. This process continues until all of the calibration data are exhausted. MPR for each cluster c is then calculated as

$$\text{MPR}_c = \frac{\sum \text{PR}_c}{N_c}, \qquad (2)$$

where MPR_c is the mean precipitation rate for cluster c, PR_c is the corresponding MW precipitation rate estimate (including zero values) of every single grid box belonging to cluster c, and N_c is the total number of precipitation and no-precipitation samples within cluster c.

Figure 4 shows a scatterplot of the MPR (y axis) versus average brightness temperature (x axis) for all 400 cluster centers used in this study. As expected, the general trend indicates that clusters with lower average brightness temperature usually correspond to higher MPR. Note that the observed relationship between a cluster's Tb and MPR is a result of considering all of the input features listed in Fig. 2. Therefore, having several distinct cluster centers with the same average Tb indicates that these clusters contain grid boxes with similar average Tb, but with different averages for the remaining input features. The clusters' MPR are used to
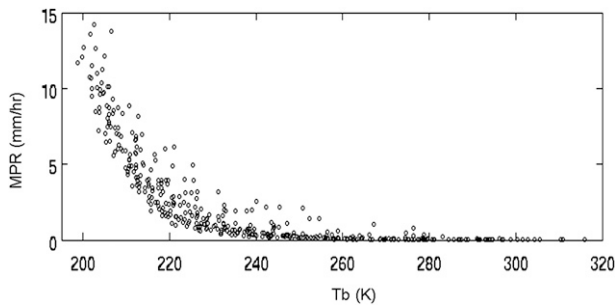
FIG. 4. Scatterplot of the MPR vs cluster average brightness temperature for all 400 clusters used in this study. Note that the location of the cluster centers is obtained via *k*-means classification using all four input features listed in Fig. 2.

adjust the advection of MW-derived precipitation estimates as described below.

c. Adjusted advection of microwave precipitation estimates along cloud advection streamlines

The final stage of the REFAME algorithm incorporates forward adjusted advection of MW-derived precipitation estimates along cloud motion streamlines obtained from GEO-IR imagery. Cloud motion vectors obtained using 2D cloud tracking are used in conjunction with cluster MPRs described in section 3a to both advect and adjust the MW precipitation field forward in time. If the location vectors along an advection streamline form a sequence X_t, $t = 1, 2, \ldots$, and the GEO satellite feature vector at location X_t is associated with a

cluster of mean precipitation rate $\mathrm{MPR}(X_t)$ then the adjusted advected microwave rain-rate $\mathrm{MW}^*(X_{t+1})$ is calculated iteratively along the streamline as

$$\mathrm{MW}^*(X_{t+1}) = \mathrm{MW}^*(X_t) \times \mathrm{Ca}(X_{t+1}), \qquad (3)$$

where

$$\mathrm{Ca}(X_{t+1}) = \frac{\mathrm{MPR}(X_{t+1}) + 1}{\mathrm{MPR}(X_t) + 1} \qquad (4)$$

is an adjustment coefficient.

Figure 5 schematically illustrates how clusters mean precipitation rate are employed to change the intensity of MW-derived precipitation along an advection streamline.

d. Extended REFAME incorporating GEO-based estimates of precipitation rate

REFAME is expected to result in superior performance compared to algorithms employing advection or cloud classification alone because of its ability to modify precipitation intensity through hybrid advection and adjustment of the MW precipitation forward in time. However, the method cannot account for precipitation events initiating and dying between two MW overpasses because Eq. (3) is a multiplicative adjustment. These events can be critical, as the life of an intense convective storm from growth to dissipation may occur in a matter of 1 h. Such events are captured by using more frequent GEO-observation of cloud-top properties. An extended
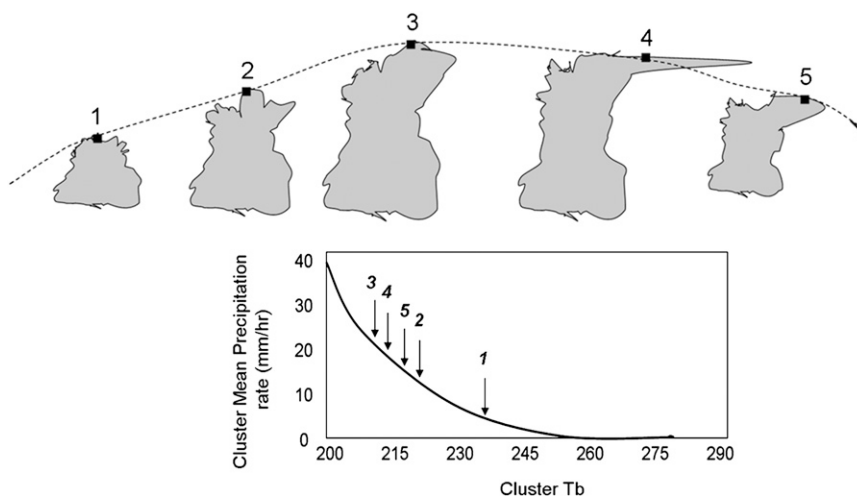

FIG. 5. Schematic demonstration of the procedure used in REFAME to modify the intensity of MW-derived precipitation as it is advected along the cloud motion streamline. Note that REFAME uses a combination of features listed in Fig. 2 and is not limited to Tb-only information for each grid box.

algorithm (REFAME-GEOmsa) has been developed to target this problem. REFAME-GEOmsa combines a GEO-IR-derived precipitation rate with that derived from REFAME by assigning proper weighs to the elements of the combination for each time-step difference from the most recent MW overpass. The development of the extended algorithm is described below.

1) GEO-IR-DERIVED PRECIPITATION RATE

As discussed in the introduction, a majority of the GEO-IR-based precipitation estimation algorithms use power-law regression or histogram-matching techniques to establish a relationship between cloud-top brightness temperature and reference precipitation measurements. The calibrated relationship is then used to estimate precipitation rate. The common result is that precipitation rate increases as cloud-top temperature decreases. However, as shown in Behrangi et al. (2009b) and Behrangi et al. (2010), the assumption does not always hold. These and other studies have demonstrated that in addition to IR brightness temperature other GEO-derived precipitation-relevant features, such as cloud texture, can improve precipitation rate estimation from GEO satellites. Although establishing a relationship between multiple features and reference precipitation rate is challenging, the method outlined in section 3a can readily incorporate multiple features, through the calculated clusters' MPR, to estimate gridbox precipitation rate. By employing a multidimensional clustering/histogram-matching technique; originally developed for multispectral precipitation estimation (PERSIANN-MSA; Behrangi et al. 2009b), GEO-IR precipitation rates are calculated from the GEO satellite feature vectors described in section 3b. In brief, clusters are assigned ranks in a descending order based on their corresponding mean rain rates (highest to lowest). In parallel, the entire rain-rate sample is also ranked in descending order. The histogram matching stage then consists of reassigning members of the rain-rate sample into the above-described clusters according to the number of samples associated with each cluster. For example, if cluster C_1 with the highest calculated mean rain rate has N_1 samples, the highest N_1 rain-rate values are reassigned to this cluster. The next highest N_2 rain-rate values are reassigned to cluster C_2 having N_2 samples, and so on for all of the clusters in the map. The rainfall estimate for a given cluster is then set equal to the mean of the samples reassigned to that cluster. Note that the use of histogram-matched rain-rate values as opposed to the original cluster means ensures that the resulting rainfall product displays a realistic dynamic range and accounts for possible mismatches between rain-rate and cloud feature locations in the calibration dataset. As with cloud classification, this technique may be readily extended to multispectral data.

2) WEIGHTED AVERAGING OF REFAME AND GEOMSA

REFAME and GEOmsa outputs were linearly combined using weights derived from a comparison of both products to a ground radar reference dataset. Figures 6a,c demonstrate that the performance of REFAME, as determined using correlation and root-mean-square error (RMSE) scores, drops as the time-distance from the previous MW overpass increases. Figures 6b,d suggest that the combination weights should be identified with respect to the time-distance from the last MW overpass. While the correlation coefficient of REFAME is more sensitive to time-distance than GEOmsa, it is less sensitive to sample counts (Figs. 6e,f), particularly as the time-distance gets larger. The large value of RMSE can be attributed to the considerable differences between MW-derived and radar precipitation estimates. Radar precipitation rates may exceed 100 mm h^{-1} as opposed to MW-derived precipitation, which does not exceed 50 mm h^{-1}. Therefore, it is expected that the uncertainty in correlation coefficient, unlike RMSE, becomes less sensitive to the existing differences in rain intensity, as the former deals with patterns and the latter deals with actual values of precipitation. While RMSE-based combination weights (Fig. 6d) could be also used, in this study COR was selected as the performance metric to assign combination weights to REFAME and GEOmsa at each time-distance (ΔT) from previous MW overpasses (Fig. 6b). The combination weights (W_{REFAME} and W_{GEOmsa}) are calculated by solving the following set of equations:

$$\frac{W_{\mathrm{REFAME}}(\Delta T)}{W_{\mathrm{GEOmsa}}(\Delta T)} = \frac{\mathrm{COR}_{\mathrm{REFAME}}(\Delta T)}{\mathrm{COR}_{\mathrm{GEOmsa}}(\Delta T)}, \qquad (5)$$

$$W_{\mathrm{REFAME}}(\Delta T) + W_{\mathrm{GEOmsa}}(\Delta T) = 1, \qquad (6)$$

where $\mathrm{COR}_{\mathrm{REFAME}}(\Delta T)$ and $\mathrm{COR}_{\mathrm{GEOmsa}}(\Delta T)$ are corresponding correlation coefficients for REFAME and GEOmsa as compared to the reference ground radar estimates at time-distance ΔT from the most recent MW estimate along the cloud motion streamlines.

Once the proper weights with respect to the time-distance from the previous MW overpass were obtained for each method, the REFAME-GEOmsa is calculated to identify the precipitation rate for each grid box as follows:

if $\Delta T \neq 0$,

$$\begin{aligned} \mathrm{PR}_{\mathrm{REFAME\text{-}GEOmsa}}(X_t) &= W_{\mathrm{REFAME}}(\Delta T) \\ &\times \mathrm{PR}_{\mathrm{REFAME}}(X_t) \\ &+ W_{\mathrm{GEOmsa}}(\Delta T) \times \mathrm{PR}_{\mathrm{GPR}}(X_t); \end{aligned}$$
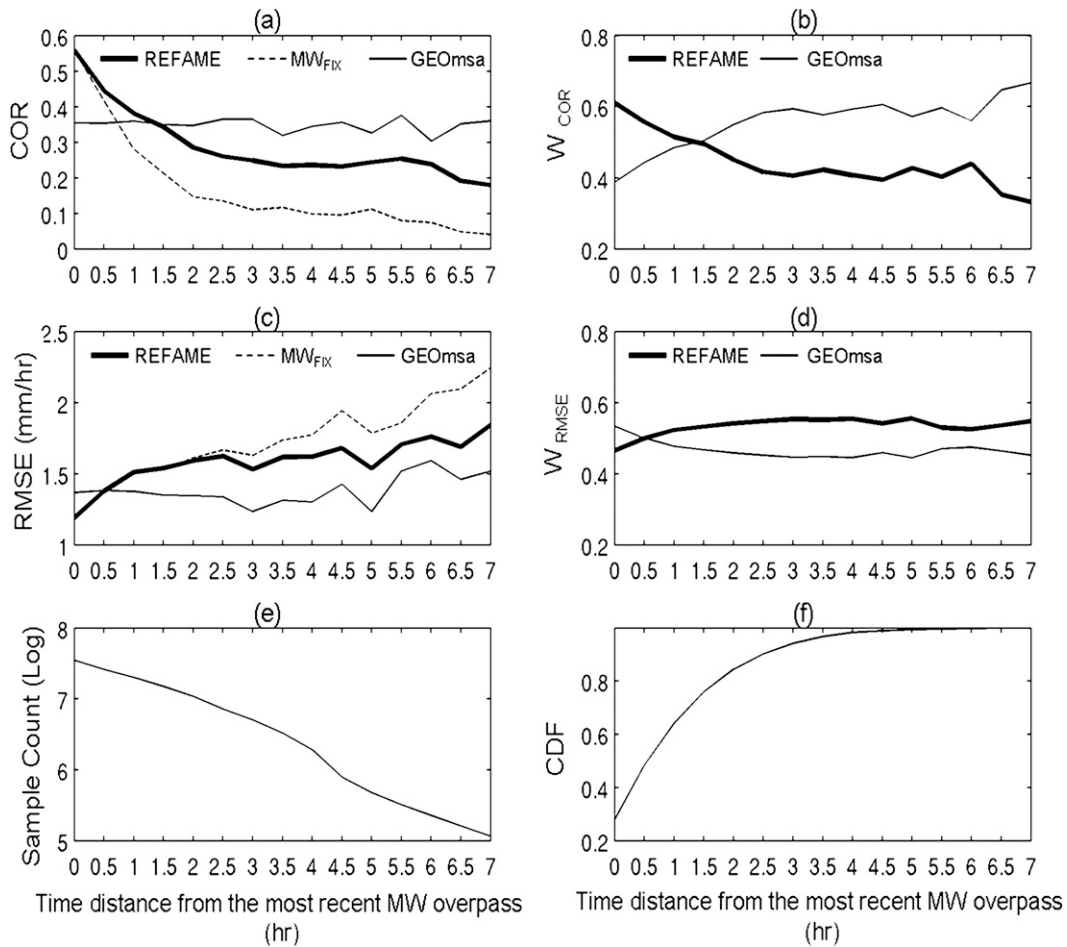$$(7)$$

Fig. 6. Analysis using the ground radar precipitating rate during the calibration period to identify combination weights to combine REFAME and GEOmsa. (a) COR of REFAME, MWfix and GEOmsa with respect to time-distance from the most recent MW overpass, (b) correlation-based combination weights (W_{COR}) for REFAME and GEOmsa, (c) RMSE of REFAME, MWfix, and GEOmsa with respect to time-distance from the most recent MW overpass, (d) RMSE-based combination weights (W_{RMSE}) for REFAME and GEOmsa, (e) number of samples collected during the calibration period to derive the statistics with respect to time-distance from the most recent MW overpass, and (f) cumulative distribution function of the sample counts with respect to time-distance from the most recent MW overpass.

otherwise,

$$PR_{REFAME\text{-}GEOmsa}(X_t) = MW(X_t), \qquad (8)$$

where $PR_{REFAME\text{-}GEOmsa}(X_t)$, $PR_{REFAME}(X_t)$, and $PR_{GEOmsa}(X_t)$ are the precipitation rate from the alternative product REFAME-GEOmsa, REFAME, and GEOmsa, respectively, at location X at time t along the cloud motion streamline.

It must be noted that in the construction of Fig. 6, the hourly radar precipitation was assumed to have occurred at uniform intensity during each interval, which may affect the correlation coefficients and RMSE values.

4. Evaluation and comparison of results

a. Model validation

REFAME is useful to investigate if inclusion of GEO-IR information can help to improve the propagated MW precipitation rate as it gets farther in time from the previous MW overpass. To assess the contributions made by the elements of the proposed adjusted-advection process, two variations of the algorithm were developed and compared to REFAME using the ground radar precipitation rate as reference:

1) Fixed MW precipitation field (MWfix).
2) Forward advection of MW precipitation field (MWadv).

In MWfix, the MW estimate of precipitation for gridbox B is kept unchanged both in location and intensity until the next MW overpass provides new precipitation estimate for B. This product was considered to provide a MW-only baseline that does not account for cloud motion, and does not use IR estimates to adjust MW estimates. MWfix, therefore, to some extent resembles the near–real time TMPA (TMPA-RT) scheme in implementing MW-derived precipitation rate in the final precipitation product. However, as described in Huffman et al. (2007) and summarized in the introduction section of the present manuscript, TMPA-RT also benefits from a MW-calibrated IR estimates to fill the remaining gaps within each time bracket of 3 h. This may lead to considerable differences between TMPA-RT and MWfix. As will be shown in the results section, MWfix can result in significant misplacement of the MW precipitation particularly when clouds are subject to rapid movement and the time-distance from previous MW overpass is large. In addition, the product cannot account for changes in rainfall intensity.

In MWadv the MW precipitation grid boxes are advected forward in time along cloud motion streamlines obtained from successive GEO-IR images using the 2D cloud motion algorithm described in section 3a. Assuming a perfect tracking of cloud grid boxes, MWadv is expected to significantly improve the positioning of MW precipitation, compared to MWfix. However, it does not account for changes in precipitation intensity between two successive MW overpasses as REFAME does. The second variation, MWadv, is tailored to be similar to the scheme implemented in CMORPH. However, as described in Joyce et al. (2004) and summarized in section 1, CMORPH also benefits from the backward propagation of the next MW-precipitation overpass to adjust the precipitation intensity at the expense of postponing the near real-time estimate of precipitation intensity for up to few hours. While by excluding the backward propagation of the next MW precipitation overpass "QMORPH" (Joyce et al. 2004) is a more timely precipitation product, REFAME was not compared to QMORPH in the present work. The main reason is QMORPH uses different tracking strategy and employs a few other adjustments that make it difficult to conclude whether the differences between REFAME and QMORPH are algorithmic or due to the variation of input features.

Evaluation of REFAME, its variations, and REFAME-GEOmsa were performed using the hourly ground radar precipitation data as "ground truth." Four evaluation statistics are used: equitable treat score (ETS), correlation coefficient (COR), RMSE, and BIAS (see the appendix for detail). ETS is computed through the construction of a binary contingency table to measure the skill of each

product in delineating rain/no-rain areas. This is attained by selecting a threshold (0.1 mm h^{-1}) above which a precipitation event is considered to have occurred. The rest of the statistical indices use quantitative values and measure how well the products can estimate rain rate compared to the reference radar rain rate. Table 1 summarizes the evaluation of 3-h aggregated rainfall products at 0.08° and 0.24° latitude–longitude resolutions. With the exception of BIAS, a performance gain/loss metric is calculated for each index to facilitate the comparison against the reference product (MWfix). The gain/loss performance metric of a given product is computed as

$$\text{Gain/Loss}_{\text{scenario}}\% = \frac{S_{\text{scenario}} - S_{\text{MWfix}}}{S_{\text{MWfix}}} \times 100. \quad (9)$$

Whether the above performance metric is considered as gain or loss depends on whether an increase or decrease of the value of the metric is better or worse. As such, obtaining a negative performance value for RMSE is gain while it is considered a loss for the rest of the evaluation indices reported in Table 1.

The results in Table 1 highlight several issues: First, by advecting the MW-derived precipitation rate (MWadv), the overall evaluation statistics with respect to the reference product (MWfix) are improved. The largest gain is reported for the correlation coefficient (~12% at 0.08° latitude–longitude and ~11% at 0.24° latitude–longitude). Second, REFAME results in significant overall improvement over both MWfix and MWadv. The improvement in COR (~23% gain at 0.08° latitude–longitude and ~21% gain at 0.24° latitude–longitude) is more remarkable than the rest of the evaluation indices. The improved correlation in conjunction with gain in RMSE (~13% at 0.08° latitude–longitude and ~14% at 0.24° latitude–longitude) implies that REFAME is very effective for both advection and adjustment of the MW-precipitation rate along the cloud motion stream lines. Third, REFAME-GEOmsa results in another significant improvement over all other products with gains in COR (~33% at 0.08° latitude–longitude and ~28% at 0.24° latitude–longitude), RMSE (~17% at 0.08° latitude–longitude and ~16% at 0.24° latitude–longitude), and ETS (~13% at 0.08° latitude–longitude and ~14% at 0.24° latitude–longitude). Fourth, all of the products capture the total volume of precipitation quite well when compared to the reference radar precipitation estimates. One major shortcoming for MWfix, MWadv, and REFAME is that they rely on the previous MW observation of precipitation field. As such, they may fail to capture the start or end of precipitation events between two MW overpasses. In contrast, the GEO-based precipitation estimation method estimates precipitation from frequent IR images, where rapid and short-lived changes in cloud-top temperature can be monitored, albeit

TABLE 1. Overall 3-h evaluation statistics during the evaluation period (16 Jul–31 Aug 2006).

	Products	ETS	ETS gain (%)	COR	COR gain (%)	RMSE mm h^{-1}	RMSE gain (%)	BIAS
0.08° lat–lon	MWfix	0.345	0.00	0.459	0.00	0.908	0.00	−0.059
	MWadv	0.353	2.17	0.514	12.14	0.855	−5.82	0.022
	REFAME	0.361	4.37	0.562	22.59	0.789	−13.08	−0.003
	GEOmsa	0.333	−3.71	0.516	12.45	0.950	4.63	0.033
	REFAME-GEOmsa	0.389	12.51	0.612	33.36	0.749	−17.44	0.006
0.24° lat–lon	MWfix	0.343	0.00	0.527	0.00	0.675	0.00	−0.079
	MWadv	0.350	1.95	0.585	11.06	0.609	−9.85	0.002
	REFAME	0.359	4.43	0.637	20.81	0.578	−14.42	−0.023
	GEOmsa	0.329	−4.17	0.564	7.08	0.835	23.60	0.013
	REFAME-GEOmsa	0.391	13.95	0.676	28.29	0.565	−16.30	−0.014

indirectly. This results in improved delineation of precipitation area as shown in Table 1 and will be displayed in the case study section.

Table 2 contains the evaluation statistics of 1-h precipitation estimates from all products at both 0.08° and 0.24° latitude–longitude resolutions. The results are consistent with the 3-h evaluation described in Table 1. Again, REFAME demonstrates the highest skill in advecting MW-derived precipitation rate forward in time with COR having been improved about 28% at 0.08° latitude–longitude and 27% at 0.24° latitude–longitude. Similarly, the weighted averaging of GEOmsa and REFAME scores the best across all other products and the gain in COR reaches about 44% at 0.08° latitude–longitude and 38% at 0.24° latitude–longitude. Table 2 also demonstrates that both REFAME and REFAME-GEOmsa can lead to substantial gain even at high time (1 h) and space (0.08° latitude–longitude) resolutions, which are favorable for hydrological applications.

Further evaluation of the correlation coefficients associated with the products studied is shown in Fig. 7. Figure 7a shows the correlation of the various products' half-hourly precipitation estimates with hourly reference radar precipitation rates with respect to time-distance from the most recent MW overpass computed at 0.08° latitude–longitude resolution. In the construction of Fig. 7, the hourly precipitation rate observation was assumed to

be uniformly distributed within each hour to allow the comparison with half-hourly precipitation rates from the various products. This results in significant reduction in COR values (e.g., the calculated correlation between hourly MW-derived and reference radar precipitation rate is about 0.75 as opposed to 0.55 obtained here). However, in relative terms, Fig. 7a clearly demonstrates the superior performance of REFAME and REFAME-GEOmsa in comparison with the reference MWfix product as well as with MWadv. REFAME-GEOmsa indicates that direct inclusion of GEO-based estimation is crucial even at small time-distances as it improves the COR significantly. Eventually, REFAME-GEOmsa approximates that of GEO-based-only precipitation estimation as less weight is assigned to REFAME (W_{REFAME}) at larger time-distances. Figure 7b shows the occurrence count (in log scale) of product–radar pairs used to derive the displayed correlations. Obviously, reduction in the counts is significant as the time gets farther from the most recent MW overpass. Figure 7c displays that the COR percent gain of products MWadv and REFAME against the reference product (MWfix) is significant. Overall, Fig. 7 clearly demonstrates that retaining the MW-derived precipitation, until the next MW overpass results in significant drop in correlation coefficient. An advection-only process progressively improves the correlation as the time-distance from previous MW overpass gets larger. The adjusted

TABLE 2. Overall 1-h evaluation statistics during the evaluation period (16 Jul–31 Aug 2006).

|	Products	ETS	ETS gain (%)	COR	COR gain (%)	RMSE mm h^{-1}	RMSE gain (%)	BIAS
0.08° lat–lon	MWfix	0.289	0.00	0.334	0.00	1.215	0.00	−0.052
	MWadv	0.295	2.29	0.384	14.90	1.184	−2.54	0.018
	REFAME	0.307	6.30	0.427	27.61	1.128	−7.15	−0.005
	GEOmsa	0.281	−2.63	0.394	17.80	1.220	0.39	0.023
	REFAME-GEOmsa	0.335	15.93	0.483	44.48	1.051	−13.48	0.002
0.24° lat–lon	MWfix	0.309	0.00	0.421	0.00	0.943	0.00	−0.072
	MWadv	0.321	3.75	0.483	14.91	0.893	−5.30	−0.002
	REFAME	0.334	8.12	0.533	26.78	0.850	−9.79	−0.025
	GEOmsa	0.292	−5.50	0.472	12.29	0.997	5.80	0.003
	REFAME-GEOmsa	0.365	17.91	0.581	38.10	0.809	−14.19	−0.019
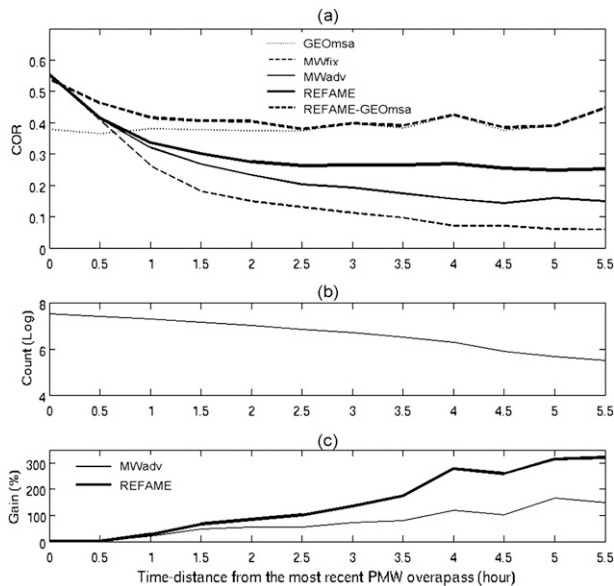
FIG. 7. Analyzing the correlation coefficient of the developed products with respect to time-distance from the most recent MW overpass. In this figure the evaluation dataset is used (16 Jul–31 Aug 2006). Hourly ground radar precipitation rate is assumed uniform in time to serve as a reference for comparing the half-hourly precipitation rates derived from different products. (a) Correlation coefficient, (b) number of available samples at each time-distance to derive the correlation coefficients reported in (a), and (c) correlation gain for MWadv and REFAME calculated from Eq. (9).

advection of the MW precipitation rate is superior to both the products with about 90% gain in correlation coefficient 2 h after the most recent MW. The improvement continues in time and as the time-distance reaches about 5 h, the gain is nearly 300% (Fig. 7c).

The above discussion focused on statistical measures that provide summaries of overall performance. It is also important to examine the performance of the various products for individual events as identified by the best matched pairs of observation/estimates. Figure 8 presents a comparison of COR and RMSE between 3-hourly, 0.24° precipitation estimates obtained from REFAME, MWfix, MWadv, and REFAME-GEOmsa and corresponding radar observations. Although the comparison covers the entire evaluation period over the full study area, 3-h radar precipitation maps associated with the lowest 10% number of rain grid boxes were excluded from the analysis to focus on extensive precipitation events. As seen in the first row, REFAME shows fairly high COR and low RMSE for a reasonable portion of the samples. When compared with MWfix and MWadv (rows 2 and 3), REFAME's COR and RMSE values demonstrate superior performance in a majority of cases as indicated by the large number of points above the 1:1 line for COR and below the 1:1 line for RMSE. The

only product with better overall performance than REFAME is REFAME-GEOmsa (bottom row).

b. Case study: Convective precipitation event

To examine the detailed workings of REFAME, a case study was investigated that covered a convective precipitation event from initiation all the way to the dissipation stage. The event, which is explored at 0.08° resolution, occurred between 0415 UTC 30 July 2006 and 1245 UTC 30 July 2006. Figure 9 shows brightness temperature (IR10.7 μm) and ground radar rain-rate maps in addition to the various satellite rainfall products. The third row displays the MW-derived precipitation maps for all available MW overpasses with missing data shown in black.

Starting at 0415 UTC, both ground radar and GEO-msa show scattered precipitation, indicating the initiation stage of the convective system. No precipitation is captured by MW, and thus no precipitation is estimated from MWfix, MWadv, and REFAME until 0815 UTC. At 0815 and 0915 an MW sensor passes over the convective system, which is already in its mature stage. Although MW and radar demonstrate major discrepancies in detecting precipitation area and estimating its intensity, both indicate that the convective system has reached to its mature state. On the other hand, the frequent observation of cloud-top Tb clearly shows the system's growth as it gradually gets colder at top and the area of the cold region gets larger. Therefore, GEOmsa and as a result REFAME-GEOmsa fairly well capture the convective growth. During the dissipation stage no MW overpass is available until 1245 UTC where the precipitation field has nearly faded. Meanwhile, MWfix and MWadv continue to show the large intense precipitation area as estimated from the most recent MW observation at 0915 UTC. However, at 1245 UTC, the large intense precipitation field is abruptly replaced by a smaller low intensity precipitation field. The observed expansion in precipitation area in MWadv (row 6) can be attributed to the ability of the 2D cloud hierarchical tracking algorithm to account for cloud divergence as discussed in Bellerby (2006). Guided by Tb observations, REFAME adjusts the MW precipitation intensities as advected along the cloud motion stream lines and demonstrates, contrary to MWFix, a fairly smooth transition toward the next MW-derived precipitation field at 1245 UTC. As expected, the dissipation trend is also captured by both GEOmsa method and REFAME-GEOmsa, which agrees with radar precipitation maps as well. By exploring the convective system two issues need to be highlighted: first, although REFAME has the ability to include GEO-IR-derived input features to adjust the MW precipitation intensities
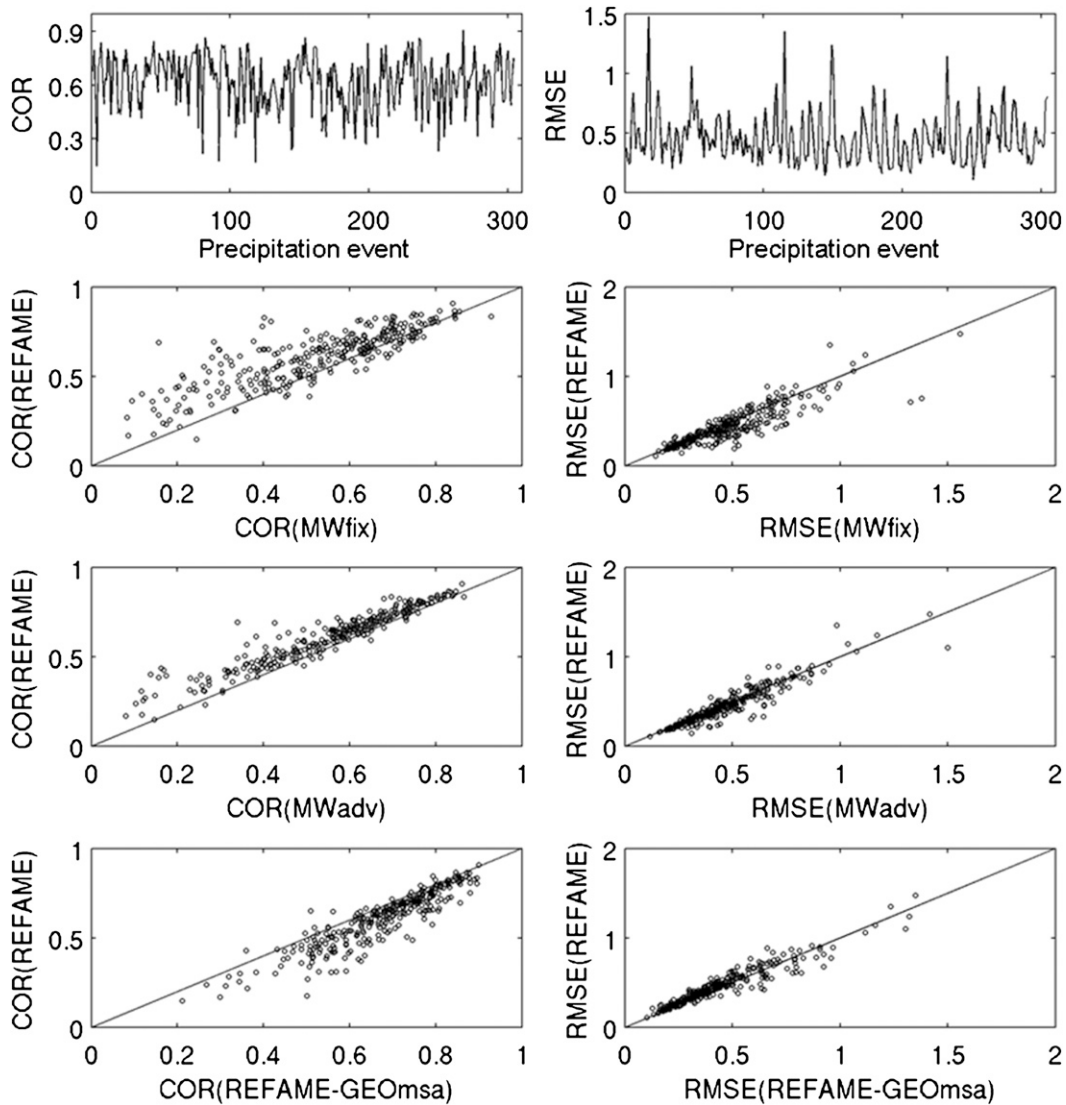
FIG. 8. The 3-h 0.24° latitude–longitude statistics over the full area of the study. (top) The (left) COR and (right) RMSE of REFAME. (from second row to bottom) Scatterplots of (left) COR and (right) RMSE for REFAME and MWfix, MW adv, and REFAME–GEOmsa.

forward in time, it cannot generate any precipitation if the most recent MW shows no precipitation. Second, REFAME-GEOmsa may ameliorate this issue if the GEO-based method captures true precipitation.

5. Conclusions

This paper described the development of REFAME, a combined IR–MW satellite rainfall estimation technique incorporating real-time adjustment of the multi-sensor MW precipitation rates as they are advected forward in time along the GEO-IR-based cloud motion streamlines. In contrast to other techniques of this type, REFAME uses cloud-classification techniques to take

account of cloud properties when deriving changes in precipitation rate along cloud motion streamlines. The method was developed and evaluated over the United States during a 3-month period of June–August 2006. To facilitate the evaluation of REFAME, two other products were developed. In the first product MW precipitation rate was held constant, while in the second product cloud advection was accounted for without adjustment of MW precipitation estimates until the next MW overpass. REFAME almost consistently outperformed these two products by demonstrating considerable gains in evaluation statistics. In addition, an extended algorithm was proposed in which REFAME was combined with GEO-derived precipitation rate through assigning weights to
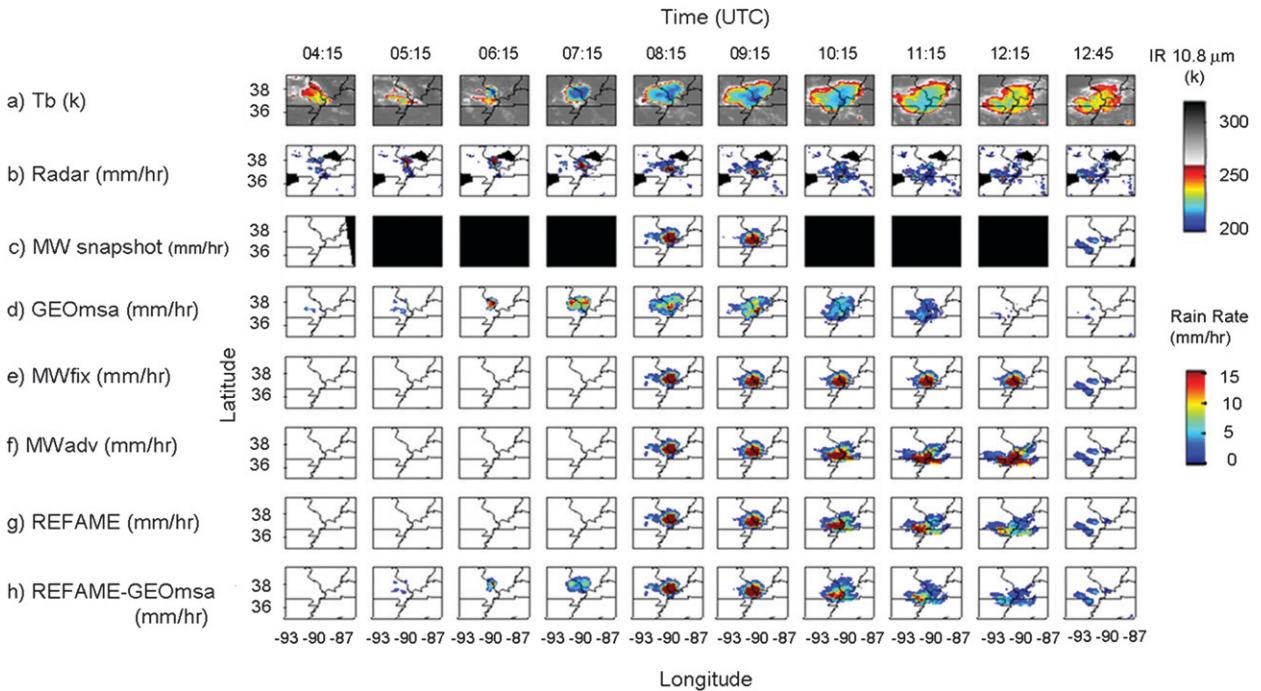
FIG. 9. Exploration of a convective precipitins system from initiation to dissipation at 0.08° resolution between 0415 UTC 30 Jul 2006 and 1245 UTC 30 Jul 2006. (a) Brightness temperature, (b) ground radar precipitation rate, (c) MW-derived precipitation rate. (d)–(h) Performances of GEOmsa, MWfix, MWadv, REFAME, and REFAME-GEOmsa, respectively. The blacked-out part in the third row indicates regions where no MW data were recorded.

each method based on time-distance from the most recent MW overpass. The main purpose of direct inclusion of GEO-based precipitation estimate was to capture precipitation events initiating and decaying during the interval between two consecutive MW overpasses. Evaluation statistics indicate that the proposed alternative performs remarkably well for real-time precipitation estimation. However, further investigation is required to assess the performance of the employed weighing-average procedures at various precipitation events.

The REFAME algorithm has been designed to readily incorporate multiple input features. As such multispectral satellite information may further improve the performance of the algorithm (Ba and Gruber 2001; Behrangi et al. 2009a,b; Capacci and Conway 2005) by virtue of improving its GEO based components. While global high temporal and spatial monitoring of cloud-top properties in visible, water vapor, and thermal IR bands are currently available from existing GEO satellites, finer spectral, spatial, and temporal resolution data is forthcoming online through the suite of recent and future geostationary satellites [e.g., Spinning Enhanced Visible and Infrared Imager (SEVIRI) on board the Meteosat Second Generation (MSG) satellite and the future Advanced Baseline Imager (ABI) on GOES-R]. Certainly, investigating potential improvements in GEO-derived

precipitation estimation using multispectral observations will continue to be an active area of research.

The REFAME algorithm can be also used in a forward–backward process such as that used in CMORPH (Joyce et al. 2004) at the expense of postponing the near-real-time precipitation estimate for a few hours. The forward–backward process will definitely improve the performance of the algorithm since it incorporates information from the next MW overpass, which, together with the previous MW information, provides better ability to capture the precipitation system's growth and decay. In reality, even a perfect IR-based cloud tracking method is unlikely to pinpoint precipitation location because of the relatively faster movement of the cloud top in comparison with the precipitation field beneath (Joyce et al. 2004). Investigating this issue is also another area of research that could lead to improvements in the presented algorithm.

REFAME demonstrates the utility of cloud-type information in determining rainfall process variation along advection streamlines. Future work could combine such classification with the precipitable water accounting of the LMODEL to derive an improved cloud-modeling-based approach.

Finally, having more accurate, frequent, and consistent MW precipitation rate should directly improve the skill of REFAME. It is hoped that the future Global

Precipitation Measurement (GPM) mission will be a significant step toward such estimates. The REFAME concept is currently under development for operational implementation. The operational product will be compared with the existing products in a future work and hopefully over the International Precipitation Working Group (IPWG) validation sites (Ebert et al. 2007).

APPENDIX

Definition of the Evaluation Statistics Used in this Study

The equitable threat score (ETS) is used to evaluate the performance of the methods in delineating the areal extent of rainfall. ETS is calculated from the binary-based contingency table that classifies the prediction outcome into the following four possibilities based on observation of rain/no-rain occurrences:

- Hits (H)—Number of pixels correctly classified as rainfall,
- Misses (M)—Number of pixels incorrectly classified as no rainfall,
- False alarms (F)—Number of pixels incorrectly classified as rainfall,
- Correct negatives (Z)—Number of pixels correctly classified as no rainfall.

ETS is computed as follows:

$$\text{ETS} = (H - \text{hits}_{\text{random}})/(H + M + F - \text{hits}_{\text{random}}),$$

where,

$$\text{hits}_{\text{random}} = [(H + M)(H + F)]/(H + M + F + Z).$$

Quantitative statistics are computed using observed (RR_{obs}) and estimated (RR_{est}) rain rates and the total number of observed and estimated rain pairs (N).

$$\text{The correlation coefficient (CORR)} = \frac{\sum_{i=1}^{N}[(\text{RR}_{\text{obs}})_i(\text{RR}_{\text{est}})_i] - [N(\overline{\text{RR}}_{\text{obs}})(\overline{\text{RR}}_{\text{est}})]}{\sqrt{\left[\sum_{i=1}^{N}(\text{RR}_{\text{obs}})_i^2 - N(\overline{\text{RR}}_{\text{obs}})^2\right]\left[\sum_{i=1}^{N}(\text{RR}_{\text{est}})_i^2 - N(\overline{\text{RR}}_{\text{est}})^2\right]}},$$

$$\text{Root mean square (RMSE)} = \left\{\frac{1}{N}\sum_{i=1}^{N}[\text{RR}_{\text{est}}(i) - \text{RR}_{\text{obs}}(i)]^2\right\}^{0.5}, \quad \text{and}$$

$$\text{Bias (BIAS)} = \frac{\sum_{i=1}^{N}[\text{RR}_{\text{est}}(i) - \text{RR}_{\text{obs}}(i)]}{N}.$$

REFERENCES

Adler, R. F., A. J. Negri, P. R. Keehn, and I. M. Hakkarinen, 1993: Estimation of monthly rainfall over Japan and surrounding waters from a combination of low-orbit microwave and geosynchronous IR data. *J. Appl. Meteor.,* **32,** 335–356.

Ba, M. B., and A. Gruber, 2001: GOES multispectral rainfall algorithm (GMSRA). *J. Appl. Meteor.,* **40,** 1500–1514.

Behrangi, A., K.-L. Hsu, B. Imam, S. Sorooshian, and R. J. Kuligowski, 2009a: Evaluating the utility of multispectral information in delineating the areal extent of precipitation. *J. Hydrometeor.,* **10,** 684–700.

——, ——, ——, ——, G. J. Huffman, and R. J. Kuligowski, 2009b: PERSIANN-MSA: A precipitation estimation method from satellite-based multispectral analysis. *J. Hydrometeor.,* **10,** 1414–1429.

——, ——, ——, and ——, 2010: Daytime precipitation estimation using bispectral cloud classification system. *J. Appl. Meteor. Climatol.,* **49,** 1015–1031.

Bellerby, T., 2006: High-resolution 2-D cloud-top advection from geostationary satellite imagery. *IEEE Trans. Geosci. Remote Sens.,* **44,** 3639–3648.

——, K.-L. Hsu, and S. Sorooshian, 2009: LMODEL: A satellite precipitation methodology using cloud development modeling.

Part I: Algorithm construction and calibration. *J. Hydrometeor.,* **10,** 1081–1095.

Capacci, D., and B. J. Conway, 2005: Delineation of precipitation areas from MODIS visible and infrared imagery with artificial neural networks. *Meteor. Appl.,* **12,** 291–305.

Dinku, T., S. Chidzambwa, P. Ceccato, S. J. Connor, and C. F. Ropelewski, 2008: Validation of high-resolution satellite rainfall products over complex terrain. *Int. J. Remote Sens.,* **29,** 4097–4110.

Duda, R., and P. Hart, 1973: *Pattern Classification and Scene Analysis.* John Wiley & Sons, 482 pp.

Ebert, E. E., J. E. Janowiak, and C. Kidd, 2007: Comparison of near-real-time precipitation estimates from satellite observations and numerical models. *Bull. Amer. Meteor. Soc.,* **88,** 47–64.

Everitt, B. S., 1993: *Cluster Analysis.* 3rd ed. Halsted Press, 170 pp.

Ferraro, R. R., 1997: Special sensor microwave imager derived global rainfall estimates for climatological applications. *J. Geophys. Res.,* **102,** 16 715–16 736.

——, F. Weng, N. C. Grody, and L. Zhao, 2000: Precipitation characteristics over land from the *NOAA-15* AMSU sensor. *Geophys. Res. Lett.,* **27,** 2669–2672.

Hong, Y., K. L. Hsu, S. Sorooshian, and X. G. Gao, 2004: Precipitation Estimation from Remotely Sensed Imagery using an Artificial Neural Network cloud classification system. *J. Appl. Meteor.,* **43,** 1834–1852.

Hsu, K.-L., T. Bellerby, and S. Sorooshian, 2009: LMODEL: A satellite precipitation methodology using cloud development modeling. Part II: Validation. *J. Hydrometeor.,* **10,** 1096–1108.

Huffman, G. J., and Coauthors, 2007: The TRMM Multisatellite Precipitation Analysis (TMPA): Quasi-global, multiyear, combined-sensor precipitation estimates at fine scales. *J. Hydrometeor.,* **8,** 38–55.

Janowiak, J. E., R. J. Joyce, and Y. Yarosh, 2001: A real-time global half-hourly pixel-resolution infrared dataset and its applications. *Bull. Amer. Meteor. Soc.,* **82,** 205–217.

Joyce, R. J., J. E. Janowiak, P. A. Arkin, and P. Xie, 2004: CMORPH: A method that produces global precipitation estimates from passive microwave and infrared data at high spatial and temporal resolution. *J. Hydrometeor.,* **5,** 487–503.

——, P. Xie, and Y. Yarosh, 2008: A Kalman filter approach to blend various satellite rainfall estimates in CMORPH. *Fourth Workshop of the IPWG,* Beijing, China, IPWG, 194 pp.

Kidd, C., D. R. Kniveton, M. C. Todd, and T. J. Bellerby, 2003: Satellite rainfall estimation using combined passive microwave and infrared algorithms. *J. Hydrometeor.,* **4,** 1088–1104.

Kuligowski, R. J., 2002: A self-calibrating real-time GOES rainfall algorithm for short-term rainfall estimates. *J. Hydrometeor.,* **3,** 112–130.

Kummerow, C., and L. Giglio, 1995: A method for combining passive microwave and infrared rainfall observations. *J. Atmos. Oceanic Technol.,* **12,** 33–45.

——, and Coauthors, 2001: The evolution of the Goddard Profiling Algorithm (GPROF) for rainfall estimation from passive microwave sensors. *J. Appl. Meteor.,* **40,** 1801–1820.

Lin, Y., and K. E. Mitchell, 2005: The NCEP stage II/IV hourly precipitation analyses: Development and applications. Preprints, *19th Conf. on Hydrology,* San Diego, CA, Amer. Meteor. Soc., 1.2. [Available online at http://ams.confex.com/ams/pdfpapers/83847.pdf.]

MacQueen, J. B., 1967: Some methods for classification and analysis of multivariate observations. *Proceedings of the Fifth Berkeley Symposium on Mathematical Statistics and Probability,* Vol. 1, University of California Press, 281–297.

Martin, D. W., B. Goodman, T. J. Schmit, and E. C. Cutrim, 1990: Estimation of daily rainfall over the Amazon basin. *J. Geophys. Res.,* **95,** 17 043–17 050.

Miller, S. W., P. A. Arkin, and R. Joyce, 2001: A combined microwave/infrared rain rate algorithm. *Int. J. Remote Sens.,* **22,** 3285–3307.

Qiu, D., and A. C. Tamhane, 2007: A comparative study of the k-means algorithm and the normal mixture model for clustering: Univariate case. *J. Stat. Plann. Infer.,* **137,** 3722–3740.

Sapiano, M. R. P., and P. A. Arkin, 2009: An intercomparison and validation of high-resolution satellite precipitation estimates with 3-hourly gauge data. *J. Hydrometeor.,* **10,** 149–166.

Sorooshian, S., K. L. Hsu, X. Gao, H. V. Gupta, B. Imam, and D. Braithwaite, 2000: Evaluation of PERSIANN system satellite-based estimates of tropical rainfall. *Bull. Amer. Meteor. Soc.,* **81,** 2035–2046.

Tian, Y., C. D. Peters-Lidard, B. J. Choudhury, and M. Garcia, 2007: Multitemporal analysis of TRMM-based satellite precipitation products for land data assimilation applications. *J. Hydrometeor.,* **8,** 1165–1183.

Todd, M. C., C. Kidd, D. Kniveton, and T. J. Bellerby, 2001: A combined satellite infrared and passive microwave technique for estimation of small-scale rainfall. *J. Atmos. Oceanic Technol.,* **18,** 742–755.

Turk, F. J., G. D. Rohaly, J. Hawkins, E. A. Smith, F. S. Marzano, A. Mugnai, and V. Levizzani, 2000: Meteorological applications of precipitation estimation from combined SSM/I, TRMM, and infrared geostationary satellite data. *Microwave Radiometry and Remote Sensing of the Earth's Surface and Atmosphere,* P. Pampaloni and S. Paloscia, Eds., VSP International Science Publishers, 353–363.

Ushio, T., and Coauthors, 2009: A Kalman filter approach to the Global Satellite Mapping of Precipitation (GSMaP) from combined passive microwave and infrared radiometric data. *J. Meteor. Soc. Japan,* **87A,** 137–151.

Vicente, G. A., R. A. Scofield, and W. P. Menzel, 1998: The operational GOES infrared rainfall estimation technique. *Bull. Amer. Meteor. Soc.,* **79,** 1883–1898.

Weng, F. W., L. Zhao, R. Ferraro, G. Pre, X. Li, and N. C. Grody, 2003: Advanced microwave sounding unit (AMSU) cloud and precipitation algorithm. *Radio Sci.,* **38,** 8068–8079.

Xu, L., X. Gao, S. Sorooshian, P. A. Arkin, and B. Imam, 1999: A microwave infrared threshold technique to improve the GOES precipitation index. *J. Appl. Meteor.,* **38,** 569–579.